Line profile analysis of an astronomical spectrograph with a laser frequency comb

2014 Res. Astron. Astrophys. 14 1037

(http://iopscience.iop.org/1674-4527/14/8/014)

RAA 2014 Vol. **14** No. **8**, 1037–1045 doi: 10.1088/1674–4527/14/8/014
http://www.raa-journal.org *http://www.iop.org/journals/raa*

Research in Astronomy and Astrophysics

Line profile analysis of an astronomical spectrograph with a laser frequency comb *

Fei Zhao[1,2,4], Gang Zhao[1], Gaspare Lo Curto[3], Hui-Juan Wang[1], Yu-Juan Liu[1,4], Liang Wang[1] and Wei Wang[1]

[1] Key Laboratory of Optical Astronomy, National Astronomical Observatories, Chinese Academy of Sciences, Beijing 100012, China; *fzhao@nao.cas.cn*
[2] University of Chinese Academy of Sciences, Beijing 100049, China
[3] European Southern Observatory, Karl-Schwarzschild-Str. 2, 85748 Garching, Germany
[4] Shandong Provincial Key Laboratory of Optical Astronomy and Solar-Terrestrial Environment, School of Space Science and Physics, Shandong University, Weihai 264209, China

Received 2014 March 18; accepted 2014 April 29

Abstract We present a study of the spectral line shape associated with a High Resolution Spectrograph on the 2.16 m telescope at the Xinglong Observing Station of National Astronomical Observatories, Chinese Academy of Sciences. This measurement is based on modeling the instrumental line shape obtained by unresolved modes from a Yb-fiber mode-locked laser frequency comb. With the current repetition rate of 250 MHz and 26 GHz mode spacing on the spectrograph, we find the absolute variation of the line center, 0.0597 pixel in the direction of the CCDs, and 0.00275 pixel ($\sim$3 m s^{-1}) for relative variation in successive exposures on a short timescale. A novel double-Gaussian model is presented to improve the quality of the fit by a factor of 2.47 in a typical single exposure. We also use analysis with raw moments and central moments to characterize the change in line shape across the detector. A trend in charge transfer efficiency can be found on the E2V 4096×4096 CCD that provides a correction for wavelength calibration aiming to reach a level of precision for radial velocity below $1\ \mathrm{m\,s^{-1}}$.

Key words: techniques: radial velocities — instrumentation: laser frequency comb

1 INTRODUCTION

The detection of exoplanets with masses comparable to the Earth that are orbiting a solar-mass star needs repeatable long-term radial velocity (RV) measurements of $\lesssim 9\ \mathrm{cm\,s^{-1}}$ or relative precision of 10^{-10}, which sets strong requirements on the stability and quality of the wavelength calibration process. Modern cross-dispersed echelle spectrographs coupled with two kinds of calibration sources (iodine absorption cell and thorium-argon (ThAr) hollow cathode lamp) have enabled the discovery of more than 550 exoplanets by measuring the stellar RV variations. In recent years, remarkable breakthroughs have been made in Exoplanetology, especially studies relying on improvements in high precision RV measurements. Examples include an Earth-mass planet orbiting α Cen B

* Supported by the National Natural Science Foundation of China.

(Dumusque et al. 2012), and Super-Earths around M-dwarf neighbors (Bonfils et al. 2013; Delfosse et al. 2013). Growing interest in low-mass exoplanets in the habitable zone makes ultra-high precision RV measurement highly desirable.

However, the current RV precision is mainly limited by instrumental precision, in which the major source of errors arises from wavelength calibration (Murphy et al. 2007; Lo Curto et al. 2012). The drawbacks of a ThAr lamp include blended lines and superimposition of many unresolved lines. The disadvantages also come from the large dynamical range in intensity of thorium and argon emission lines that could generate fitting errors when determining the line's centroid. Its limited lifetime as an active element should also be taken into account. Moreover, another widely used calibration source, iodine cells (Marcy & Butler 1992), has a relatively narrower wavelength range (5000–6500 Å) and it significantly 'pollutes' the signal-to-noise-ratios (SNRs) by absorbing nearly half the light from the object.

Given the disadvantages of the currently available calibration sources, an ideal spectral reference is required. A laser frequency comb (LFC) (Steinmetz et al. 2008; Li et al. 2008; Braje et al. 2008) shows promise in that it can fulfill most of the key requirements for high precision and stability in wavelength calibration needed in the future, opening a new era of high-precision RV measurement with more possible applications such as measurement of variations in the fundamental constants (Webb et al. 1999; Reinhold et al. 2006; Beringer et al. 2012) and direct measurement of the Universal expansion rate (Liske et al. 2008). Compared to a traditional ThAr lamp (several tens of centimeters in RV precision or relative precision of 10^{-9}), for example, an LFC can provide thousands of reference lines with uniformity in line intensity and stable line spacing (e.g. three times the full width at half maximum (FWHM)) in the required wavelength range over a relatively long-term timescale.

In the time domain, the mode structure of a frequency comb can be expressed in terms of the electric field

$$C(t) = E(t)\,\mathrm{e}^{-j2\pi f_0 t} = \sum_n E_n\,\mathrm{e}^{-j2\pi(n\cdot f_r + f_0)t}\,, \tag{1}$$

where $E(t)$ is the envelope function and $f_r = 1/T$ is the repetition rate of the laser. T is the round trip travel time of a pulse, E_n is the nth Fourier component of the envelope $E(t)$ and f_0 is the initial frequency in the laser cavity. In general, the nth mode can be expressed as

$$f_n = f_{\mathrm{ceo}} + n \cdot f_r\,, \tag{2}$$

where n is an integer number (typically a large number) that scales the frequency from the radio wavelength range into the optical domain, and f_{ceo} is the carrier envelope offset frequency. The stability of an LFC is based on techniques (e.g. a phase-locked loop) employed to stabilize it to an atomic clock in the radio frequency domain. When an LFC based on a Yb-fiber laser is applied to an astronomical spectrograph (e.g. $R \sim 50\,000$), there are some more steps that need to be developed. Firstly, the central wavelength (10 300 Å) needs to be frequency-doubled to the visible domain around 5200 Å in which most stellar absorption lines for the target are located. Secondly, the typical 250 MHz repetition frequency (or mode spacing) cannot be directly resolved by an available spectrograph. A spectral filter is required to suppress an integer number of intermediate comb lines, depending on the resolution of the spectrograph and the corresponding point spread function. For instance, a line spacing around $\sim$3 times the resolution (or FWHM) tends to be appropriate for the spectrograph, when assuming a typical Gaussian-like instrumental profile (IP). Last but not least, we need to extend the wavelength coverage and broaden the LFC spectrum. Given a certain line spacing, the larger wavelength coverage could provide more reference lines and can significantly increase the final RV precision.

In this context, a program demonstrating the utility of a mode-locked Yb-fiber LFC as the wavelength calibration source coupled to the High Resolution Spectrograph (HRS) on the 2.16 m telescope at the Xinglong Observing Station of National Astronomical Observatories, Chinese Academy

of Sciences (NAOC), began in 2013. The collaboration between NAOC and Peking University has produced fruitful test campaigns and useful data for analysis. The HRS is a fiber-fed cross-dispersed echelle spectrograph mounted on the coudé focal plane of the 2.16 m telescope. The wavelength coverage is designed to cover the range from 3800 Å to 7500 Å. The resolution of the spectrograph is determined by a slit with width (0.19 mm) or the diameter of the fiber ($2.4''$), with a typically available value of R ∼49 800. At this resolution, each spectral element is sampled by ∼3.4 pixels on average. The detectors are two $2\mathrm{k} \times 4\mathrm{k}$ CCDs with 49.2 mm^2 area and each pixel size is 12 μm. Currently with the averaged RV precision of ∼6 $\mathrm{m\,s^{-1}}$ based on the iodine absorption cell and using the ThAr lamp as a wavelength reference, the HRS has found several brown dwarfs and substellar companions (Liu et al. 2008, 2009; Wang et al. 2012) as well as providing significant contributions to the East-Asian Planets Search Network (EAPSNET) (Izumiura 2005).

In this paper, we start by briefly introducing the instrumental setup for an LFC (Sect. 2), and then the data reduction process is described. After that, we proceed by presenting various fitting models for the instrumental line shape (Sect. 3). We also perform the raw moment and central moment analysis for the extracted spectra (Sect. 4). Finally, by comparing models, we give a discussion of the line shape variation and characterize the corresponding effects to improve the RV measurement with this spectrograph that incorporates the LFC (Sect. 5).

2 INSTRUMENTAL SETUP

A Yb-fiber laser acts as the comb signal generator with a repetition frequency of 250 MHz. The fiber amplifier is employed to generate sufficient power for driving the following second harmonic generator which doubles the frequency centered in the optical wavelength range (5760 Å, measured with reduced data). After this, the light is injected into the photonic crystal fiber for spectral broadening. For the current test campaigns, we have the final available wavelength range of about 400 Å (5556 Å ∼5967 Å). Then the spacing between each mode is increased with Fabry-Pérot Cavities (FPCs). One FPC was used in December 2013, aiming to test the comb line at several intensity levels and to investigate the various fitting models for line shape skewness, since the side-mode effect could slightly affect each neighboring mode. In the test campaigns, our FPC has a radius of curvature of –200 mm with reflection of 99.2%. The current finesse is 390 and linewidth is 30 GHz/390 = 76.9 MHz. When $f_{\mathrm{rep}} = 250$ MHz, the side-mode suppression ratio is 2.3% with the corresponding signal to noise ratio (SNR) of 16.38 dB. A higher repetition frequency has also been tested. With $f_{\mathrm{rep}} = 500$ MHz, we can measure the side-mode suppression ratio of 0.57% and SNR of 22.44 dB. For real routine observations in the near future, two or three FPCs are required to clean every sub-mode signal between each neighboring comb line. In the following, a fiber shaker and double imaging scrambler are installed to increase the modes' spatial occupation, and remove the multi-pass interference effect. Finally, the light is projected into the HRS and illuminates echelle orders from 36 to 47. A detailed setup of the system is shown in Figure 1. We choose eight orders (38 to 45) with higher spectral quality with a typical 60 s exposure for the following analysis.

3 CHARACTERIZING THE LFC ON HRS BY FITTING THE INSTRUMENTAL LINE SHAPE

In order to have a better understanding of the variation in the instrumental profile in pixel space across the detector, we model the comb lines with their original counts on each pixel. The minimization algorithm used for nonlinear least squares fitting of χ^2 is based on the standard Levenberg-Marquardt method. In this context, we define the instrumental line shape as the profile (flux is integrated by an aperture perpendicular to the spectral direction) of an infinitely narrow line passing through the spectrograph. Typically, a -7 pixel to $+7$ pixel aperture size is appropriate for the HRS orders. Considering that the LFC modes are absolutely unresolved by HRS ($R \sim 50\,000$), each comb line is narrow enough to respectively represent the instrumental line shape at its own wavelength.

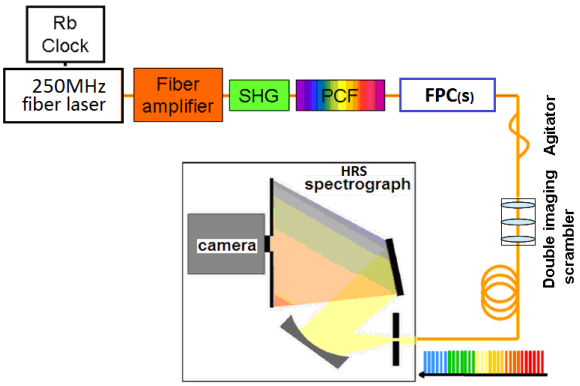

Fig. 1 A sketch of the experimental set-up for the LFC mounted on HRS. By passing through the amplifier, frequency-doubling and spectral broadening process, the initial signal with 250 MHz repetition frequency is filtered with one Fabry-Pérot Cavity, generating a mode spacing of $f' = 26$ GHz. Before injecting into the spectrograph, a fiber shaker (optional) and scrambler are employed.

For each pixel i along the spectral direction, the obtained flux F_i (in units of ADU counts) can be described as a function of pixel position

$$F_i = \int_{i-1/2}^{i+1/2} E(x) \sum_{y \pm A} C(x) dx \approx E_i \cdot \int_{i-1/2}^{i+1/2} \sum_{y \pm A} C(x) dx \,, \tag{3}$$

where x is along the spectral direction and y is along the spectrum's spatial direction. A is the semi-size of the aperture for each order (typically $A = 7$). $C(x)$ is the comb function in pixel space and $E(x)$ is the envelope function. After removing the flat-field profile, $E(x)$ of the comb itself changes slowly along the spectral direction. For a tolerance that ignores the variation of the envelope function, the function above can be approximately simplified. As is well known, the LFC lines can represent the IP across the detector, so the comb function $C(x)$ can be written as the sum of IPs

$$C(x) = \sum_{n=1}^{N} \mathrm{IP}(x_n) \,, \tag{4}$$

where N is an integer whose value is determined by the spectral resolution, that is related to line spacing, and the detector size. Our aim is to find the best fitting function which can express $C(x)$ with the smallest χ^2 along the spectral direction.

Figure 2 illustrates a portion of LFC modes for a single exposure of 60 s, which is located in echelle order 41 around the center of the detector in the spectral direction. The data are from the extracted 1-D spectra after being bias subtracted or flat-field corrected.

With regards to the ideal situation or a simulation without noise input, a Gaussian profile works well when we ignore the intra-pixel sensitivity variations (IPSv) (Toyozumi & Ashley 2005). However, in the real measurement, instrumental drifts, detector noises, etc. could pollute the symmetric IP and make them have an asymmetric line shape with skewness. We use the error function times the Gaussian, Voigt and Moffat functions (marked as Ge, Ve and Me respectively) to generate a skewness factor. Another approach is to use two Gaussian components summed together with constrained initial conditions (a Constrained Double Gaussian model, or CDG). In this context, we restrict $A_1 > A_2$ and $1 < \sigma_{1,2} < 3$ to make all the fitting results convergent. In the upper panel of Figure 2, the black solid line is the curve that is fit to the Gaussian, and the dashed line is from

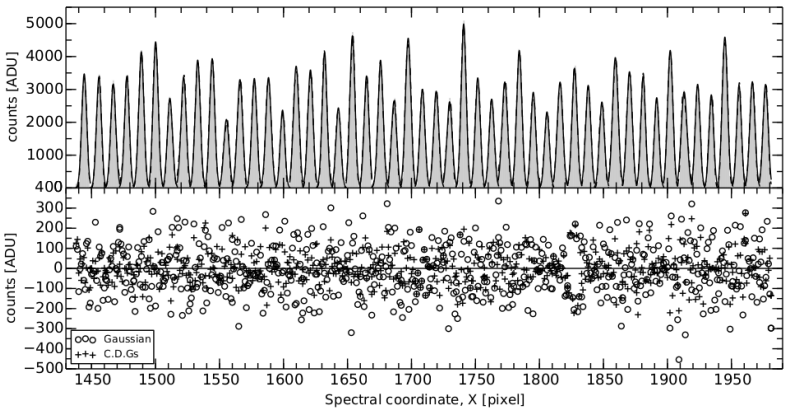

Fig. 2 A section of consecutive LFC modes on 41 echelle orders by using a Gaussian fitting model (*solid line*) and a CDG model (*dashed line*). The bottom panel shows the residuals of the two fits (with 3σ clipping). The CDG fit has a standard deviation of fitting residuals $\sim$0.51 times that of the traditional Gaussian model making the CDG better.

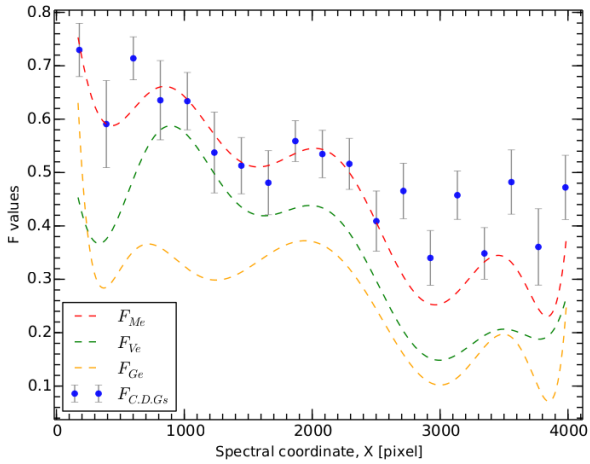

Fig. 3 A comparison of four improved asymmetric fitting models across the detector. The Moffat $\times$ error model and CDG model have higher average F (0.497 and 0.411) than the Ge and Ve models. The data points are plotted by binning the pixel axis.

the CDG model. The difference between the two fitting curves is hardly distinguishable by eye. The bottom panel of Figure 2 shows the residuals of the two fitting methods (with a 3σ clipping). For these consecutive comb lines, the standard deviation (STD) of the Gaussian model is 158.59 pixel, while it is 80.44 pixel for the CDG model. In terms of the whole order, taking echelle order 41 (347 comb lines) for example, the STD of the Gaussian is 152.93 pixels compared to 61.96 for the CDG model.

$$F = (S_1/\mathrm{DF}_1 - S_2/\mathrm{DF}_2)/(S_1/\mathrm{DF}_1). \tag{5}$$

Figure 3 shows the F distribution which evaluates the goodness of fit. S_1 is the residual sum of squares for the Gaussian fitting model, while S_2 stands for the residual sum of squares for the Ge,

Ve, Me and CDG models. DF is the number of degrees of freedom for each fitting model. There is a general trend for all the four fitting models with skewness, which is that the value of F decreases as we move from 0 to 4096 pixels in the spectral direction. We already know that the serial register is located in the right panel of Figure 3. In addition to changes in signal strength, this trend provides evidence that the charge transfer efficiency (CTE) can distort the instrumental line shape depending on if the line position is far from or close to the serial register.

4 MOMENT ANALYSIS

An analysis using the first raw moment and second and third central moments is applied to the data of a typical 60 s exposure with eight echelle orders as described above. Moment analysis can provide us raw information from the pixels without the fitting errors that occur during the minimization of the fitting process. Basically, the first raw moment determines the centroid of the line and the square root of the second central moment gives the FWHM of each comb mode. The third central moment is an indicator of skewness in the line shape. In this context, we can measure each line's first moment to probe the average drift of the line center. For example, compared to the Gaussian fit of the center, the test exposures have an average of 0.0597 pixel drifts (see in Table 1), which correspond to RV$\sim$70 $\mathrm{m\,s^{-1}}$.

Table 1 Moment analysis of 10 successive exposures. The values of moments are averaged from all the available comb lines in each acquisition and the unit is pixels.

Exposure series	First moment	$\mathrm{Error_{1st}}$	Second moment	$\mathrm{Error_{2nd}}$	Third moment	$\mathrm{Error_{3rd}}$
0	–0.01392	0.02392	3.47324	0.02176	0.21566	0.01077
1	0.02113	0.01987	3.5577	0.01384	0.19426	0.00935
2	–0.02585	0.01817	3.53944	0.0151	0.21571	0.00867
3	–0.00794	0.01708	3.58958	0.01452	0.21087	0.00799
4	–0.03708	0.01437	3.55795	0.01112	0.21845	0.00674
5	–0.03380	0.01635	3.56352	0.01227	0.21433	0.00774
6	–0.04055	0.01543	3.57412	0.01207	0.21952	0.00699
7	0.0366	0.02323	3.50331	0.01808	0.19172	0.00985
8	0.08972	0.02209	3.60285	0.02016	0.17593	0.00966
9	0.1506	0.03645	3.5617	0.03811	0.26491	0.01118

In Table 1, the last acquisition shows a relatively large drift (2.52σ). The reason for this large drift is that we turned off the air conditioning system to conduct the test during this period. Variation in temperature or pressure from the environment can lead to RV errors of several tens of meters per second. However, when we only investigate the first nine successive acquisitions under the same conditions of temperature and pressure, a drift level below 0.04 pixel can be obtained. For instance, if we pick out three connected exposures (series No. 4 to No. 6 in Table 1), their standard deviation can reach 0.00275 pixel which corresponds to an RV drift of about 3.61 $\mathrm{m\,s^{-1}}$. We can also measure how the line shape varies across the detector by investigating the third central moment γ (Fig. 4). In the first 1024 pixels on the CCD, there are less samples due to a poor SNR in this exposure. If we only include pixels from 1024 to 4096 in the analysis, γ declines from 0.099 to –0.089, which is strong evidence for a CTE-like effect on the detector (considering that the serial register is located on the right side of the CCD in the traditional plotting direction).

On the other hand, the determination of the line center for the reference source is significant for the RV measurement, especially when the line profile is asymmetric. For example, in echelle order 41 from a typical acquisition that is well illuminated, there are 347 detected comb lines in which 239 lines (68.9%) whose CDG model has better rms of fitting residuals than the traditional Gaussian model. For the Moffat $\times$ error model, the ratio is 49.3%, for the Voigt $\times$ error model it is 30.5%, and for the Gaussian $\times$ error function it is 18.7%. This means the advanced fitting models (such as

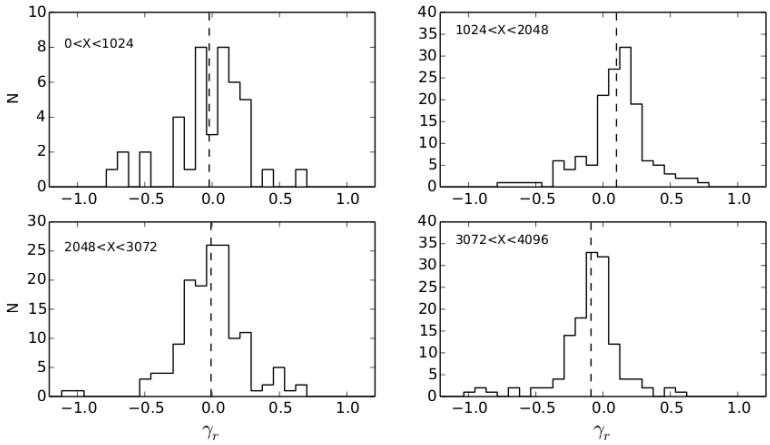

Fig. 4 The distribution of the third central moment (γ) in each 1024 range across the detector. From 0 to 1024, the mean of γ is -0.022 with a standard deviation of 0.27. The following 1024 pixel range has $\gamma_{\rm mean} = 0.099$ and $\gamma_{\rm std} = 0.23$. From 2048 to 3072 the $\gamma_{\rm mean}$ decreases to -0.0084 ($\gamma_{\rm std} = 0.25$) while in the last 1024 pixels the $\gamma_{\rm mean}$ declines to -0.089 with $\gamma_{\rm std} = 0.23$. The data used here are only from echelle orders 40, 41 and 42.

CDG) assign better weights to the asymmetric parts of modes, which can be seen as the extra tail in each comb mode. The varying instrumental line shape can also be revealed by the second central moment M_2, especially when we compare it to the corresponding σ that comes from fitting various models.

Figure 5 demonstrates a simple Gaussian profile with the measured M_2. An asymmetric shape can be immediately characterized when we reference the simulated trend. The other correlation is depicted in Figure 6. The data are also from 347 comb lines in order 41. Since the spectrum's space direction (y) is less important than the main dispersion direction (x), order 41 that is well illuminated across pixels $\sim$0 to 4096 pixel can represent the variation of a standard sample. We should also highlight that the case Moffat $\times$ error has the largest area on which light is scattered (Fig. 6), which provides wide ranges of compensations for the asymmetric line shape component, providing better fitting residuals than other models.

Additionally, in order to test the stability of the HRS-LFC system, we measure the mean of the relative drift of the first raw moment by successively acquiring 10 successive exposures. Our current test only covers a short timescale but we can achieve a precision of 3.61 m s^{-1} from three consecutive acquisitions. The other test exposures are mainly affected by the variation of temperature and pressure in the coudé room, giving relatively large drift with a value beyond 3σ.

5 CONCLUSIONS

We describe a series of successful tests using a 250 MHz Yb-fiber laser frequency comb coupled to the HRS on the 2.16 m telescope at the Xinglong Observing Station, NAOC. By using one FPC, we disperse the available 26 GHz mode spacing comb over more than 13 echelle orders (5556 Å $\sim$5967 Å) on the HRS. We choose several higher quality orders and exposures for analysis of the instrumental line shape. Four asymmetric models are presented showing significant improvements beyond the traditional Gaussian profile. Among these, a novel CDG model gives the best fitting results so far. Analysis of the first raw moment and the second and third central moments is applied to the spectra, which aims to characterize variations in the line shape.

As we detected and measured skewness and variation in the instrumental line shape, the following question is where these errors and noise come from and how we can remove or correct them.

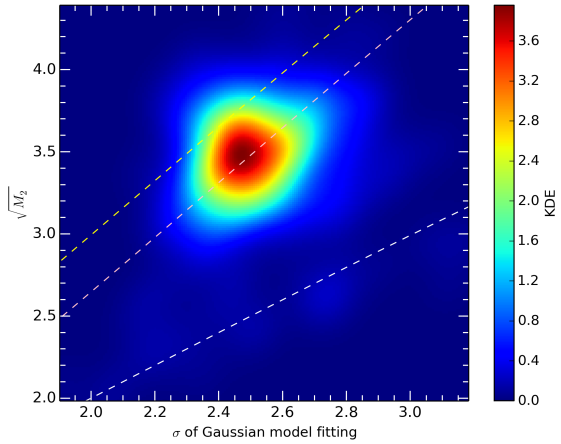

Fig. 5 The Gaussian Kernel Density Estimation (KDE) for the correlation between the square root of the second central moment ($\sqrt{M_2}$) and σ of the Gaussian profile model. Three dashed line are numerical simulations based on different fitting models. The bottom dashed line is based on a perfectly symmetric Gaussian profile digitalized by $\mathrm{FWHM} = 3$. The upper dashed line is from the Gaussian $\times$ error model with the error function's amplitude $A_\mathrm{e} = 2$ and center $\mu_2 = 1$. The middle dashed line comes from the same model but with $A_\mathrm{e} = 2$ and center $\mu_2 = 0.5$.

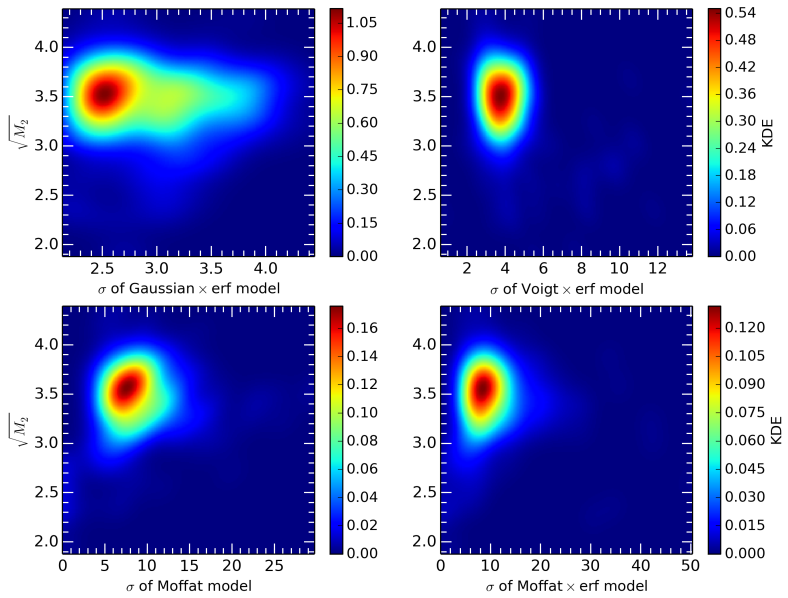

Fig. 6 KDE density image for the four fitting models: 'Ge,' 'Ve,' 'M'and 'Me.'

Basically, we think that the error sources include: (i) The effect of the sub-modes has not been completely filtered out by FPCs. In the future, this could be resolved by adding another one or two FPCs to suppress all the possible sub-modes and increasing the mode spacing. (ii) The scrambling and shaker units in the light path need to be updated to efficiently increase the modes' spatial occupation. (iii) The area where light is collected may not be very stable so that a slight change could alter

the line profile. A more stable area for collecting light could be used in the future to control and hopefully remove this effect. (iv) The relatively low SNR is another important limit for the stability of the measured line shape. When signals suffer very low SNR levels, background noises tends to dominate the line shape, making it necessary to extend the exposure time and obtain higher SNR data. (v) Considering effect from the detector, such as CTE (Bouchy et al. 2009), our moment analysis provides evidence for the existence of this behavior when charge transfers across the detector during the CCD readout. (vi) IPSv (Toyozumi & Ashley 2005; Murphy et al. 2012) are another noticeable effect affecting the instrumental line shape. Currently there is no strong evidence for this on the CCD connected to the HRS, but since the LFC routinely acts as a wavelength calibration source, the IPSv should also be corrected. (vii) External factors in the environment can also generate RV drifts of several tens of meters per second. Strict temperature and pressure controls will be performed in the following observations with LFC as a wavelength reference.

As we can see from the above, LFC is not only a novel tool which opens the possibility of investigating many RV error sources that have never been seen or detected before, but more importantly the HRS-LFC system can also hopefully provide repeatability in RV measurements that are 6–10 times better than now, potentially yielding more low-mass exoplanets.

Acknowledgements We would like to thank the team and staff of Peking University (State Key Laboratory of Advanced Optical Communication System and Networks, School of Electronics Engineering and Computer Science) for their efforts and help to this work. We are grateful to the staff at the Xinglong Observing Station for their supports during tests of the instrument. This work is supported by the National Natural Science Foundation of China (Grant Nos. 11233004 and 11390371). This project is also supported by the Specialized Research Fund for Shandong Provincial Key Laboratory.

References

Beringer, J., Arguin, J.-F., Barnett, R. M., et al. 2012, Phys. Rev. D, 86, 010001

Bonfils, X., Lo Curto, G., Correia, A. C. M., et al. 2013, A&A, 556, A110

Bouchy, F., Isambert, J., Lovis, C., et al. 2009, in EAS Publications Series, vol. 37, ed. P. Kern, 247

Braje, D. A., Kirchner, M. S., Osterman, S., Fortier, T., & Diddams, S. A. 2008, European Physical Journal D, 48, 57

Delfosse, X., Bonfils, X., Forveille, T., et al. 2013, A&A, 553, A8

Dumusque, X., Pepe, F., Lovis, C., et al. 2012, Nature, 491, 207

Izumiura, H. 2005, Journal of Korean Astronomical Society, 38, 81

Li, C.-H., Benedick, A. J., Fendel, P., et al. 2008, Nature, 452, 610

Liske, J., Grazian, A., Vanzella, E., et al. 2008, MNRAS, 386, 1192

Liu, Y.-J., Sato, B., Zhao, G., & Ando, H. 2009, RAA (Research in Astronomy and Astrophysics), 9, 1

Liu, Y.-J., Sato, B., Zhao, G., et al. 2008, ApJ, 672, 553

Lo Curto, G., Manescau, A., Avila, G., et al. 2012, in Society of Photo-Optical Instrumentation Engineers (SPIE) Conference Series, vol. 8446

Marcy, G. W., & Butler, R. P. 1992, PASP, 104, 270

Murphy, M. T., Locke, C. R., Light, P. S., Luiten, A. N., & Lawrence, J. S. 2012, MNRAS, 422, 761

Murphy, M. T., Udem, T., Holzwarth, R., et al. 2007, MNRAS, 380, 839

Reinhold, E., Buning, R., Hollenstein, U., et al. 2006, Physical Review Letters, 96, 151101

Steinmetz, T., Wilken, T., Araujo-Hauck, C., et al. 2008, Science, 321, 1335

Toyozumi, H., & Ashley, M. C. B. 2005, PASA, 22, 257

Wang, L., Sato, B., Zhao, G., et al. 2012, RAA (Research in Astronomy and Astrophysics), 12, 84

Webb, J. K., Flambaum, V. V., Churchill, C. W., Drinkwater, M. J., & Barrow, J. D. 1999, Physical Review Letters, 82, 884